

MASS LOSS FROM OH/IR STARS: MODELS FOR THE INFRARED EMISSION
OF CIRCUMSTELLAR DUST SHELLSK. JUSTTANONT^{1,2} AND A. G. G. M. TIELENS¹

Received 1991 July 1; accepted 1991 September 27

ABSTRACT

We have modeled the infrared emission of a sample of 24 OH/IR stars deriving the properties of circumstellar dust and mass-loss rate of the central star. Our results show that for some sources the observations of the far-infrared emission is well fitted with a λ^{-1} law, while some have a steeper index of 1.5. At 60 μm , this corresponds to κ_{60} of 240 and 160 $\text{cm}^2 \text{g}^{-1}$ for the former and latter, respectively. For a few sources, detailed studies of the observed 10 μm feature suggest the presence of circumstellar ice grains. Dust mass-loss rates have been determined from detailed studies for all the stars in this sample. They range from $6.0 \times 10^{-10} M_{\odot} \text{yr}^{-1}$ for an optically visible Mira to $2.2 \times 10^{-6} M_{\odot} \text{yr}^{-1}$ for a heavily obscured OH/IR star. These dust mass-loss rates are then compared to those calculated from *IRAS* photometry using 12, 25, and 60 μm fluxes. The dust mass-loss rates are also compared to gas mass-loss rates determined from OH and CO observations. For stars with tenuous shells, a dust-to-gas ratio of 0.001 is obtained. For heavily obscured stars, however, both OH and CO seem to underestimate the mass-loss rate considerably. This may be due to a recent ($< 10^2$ yr) enhancement in mass-loss rates.

Subject headings: dust, extinction — radiation mechanisms: thermal — stars: giant — stars: mass-loss

1. INTRODUCTION

The last stages of evolution of low-mass ($\leq 8 M_{\odot}$) stars is governed by mass loss (de Jong 1983; Iben & Renzini 1983, and references therein). Observations with the *Infrared Astronomical Satellite (IRAS)* have revealed a great deal on stellar mass loss during these phases. Thousands of stars were observed to have infrared excess, due to circumstellar dust which forms in the outflow of the stars on the Asymptotic Giant Branch (AGB). Circumstellar dust can be used to class stars into two groups according to the relative abundances of carbon and oxygen. For carbon-rich stars, the low-resolution spectrometer (LRS) spectra show a feature at 11.3 μm due to SiC, while oxygen-rich stars have signatures of silicate at 9.7 and 18 μm .

Wilson & Barrett (1968) reported the first detection of OH masers toward many infrared sources which were identified as long-period variables. The OH maser is pumped by infrared emission from the circumstellar dust shell (Elitzur, Goldreich, & Scoville 1976). Systematic surveys have revealed that OH maser emission is a common phenomenon for AGB stars (e.g., Bowers 1978; Baud et al. 1979; te Lintel Hekkert et al. 1989). These OH/IR stars are in the last stage of stellar evolution when mass is being lost at a very high rate. The central stars of many of these objects cannot be seen due to the thick circumstellar envelopes. However, studies of the infrared emission of these dust shells are valuable in understanding the nature and evolution of these sources. In particular, the mass-loss rates and the properties of the circumstellar dust can be determined this way (e.g., Rowan-Robinson & Harris 1983; Bedijn 1987; Kwok 1988).

Here we report the results of an analysis of the infrared emission from a sample of OH/IR sources associated with AGB stars, which span a wide range in properties of the cir-

cumstellar shell. The details of the method are presented in § 2. The results of detailed model fits to the observed infrared emission are presented in § 3. The derived dust mass-loss rates are compared to those determined from other methods, as well as gas mass-loss rates in § 4. Finally, the conclusions are summarized in § 5.

2. PROCEDURE

2.1. Radiative Transfer Code

The program used to calculate the emergent flux from a star is described in full by Haisch (1979). It solves radiative transfer through a spherically symmetric dust shell using a generalized two-stream Eddington approximation. The code can accommodate multiple grain sizes and multiple grain components. In this scheme, a circumstellar envelope is divided into many thin shells, and the emergent flux is calculated through each radius, taking into account the effects of nonisotropic scattering, absorption, and thermal reemission. The code solves for the radiation field by an iterative method, with each iteration leading to a new temperature distribution for each grain size throughout the shell which is consistent with the radiation field. Such a calculation for a two-grain model has been done for the carbon-rich star, IRC + 10216 (Griffin 1990) where the two components are silicon carbide and amorphous carbon. For the oxygen-rich stars modeled in this paper, the grains used are silicate and silicate core-ice mantle grains. The numerical calculations included 20 grain sizes ranging from 0.005 to 0.25 μm , 80 frequency points, and up to 400 radial grid points for a very optically thick dust shell.

2.2. Grain Parameters

Optical constants for silicate grains have been given by Draine & Lee (1984). However, we have replaced the 10 μm feature using the results from Kratschmer & Huffman (1979) because it provides a better fit to the observed spectra. Mie theory was used to calculate the extinction coefficient, $Q(\text{ext})$, at each wavelength, together with the albedo and phase func-

¹ NASA Ames Research Center, MS 245-3, Moffett Field, CA 94035.

² University College London, Department of Physics and Astronomy, Gower Street, London WC1E 6BT, England, UK.

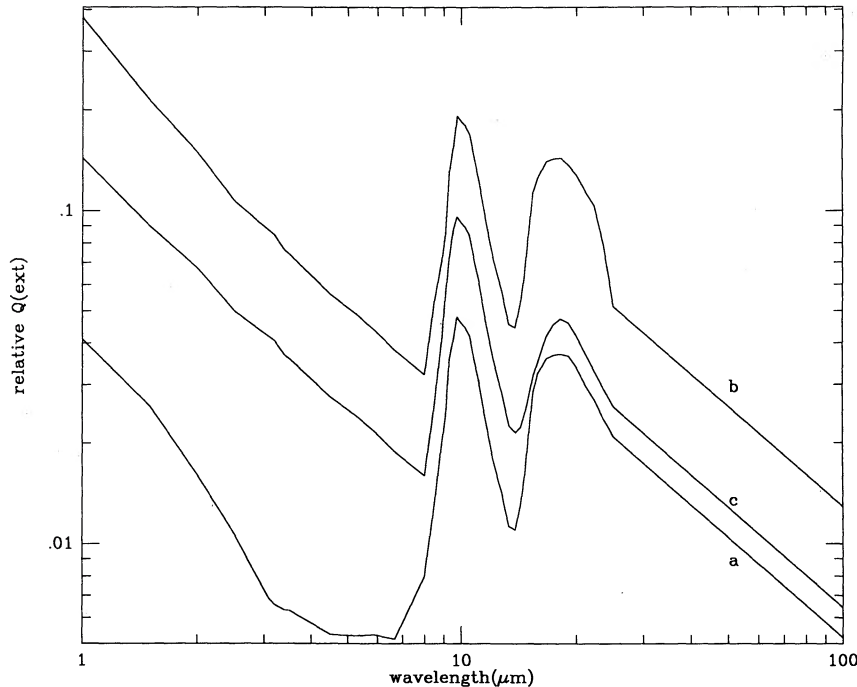


FIG. 1.—Adopted extinction coefficients for silicate grains for three sets of models with the index for far-infrared efficiency, $p = 1$. (a) For OH 26.5+0.6; (b) for AFGL 230; (c) for the rest of the stars. Peak strength of 20:10 μm is 0.8 for (a) and (b) and 0.5 for (c).

tion (van de Hulst 1981). The 10 μm feature was scaled to a ratio of 20:10 μm peak extinction of 1:2 (see Bedijn 1987). In two cases, AFGL 230 and OH 26.5+0.6, the shape of the 10 μm feature required further modification. This was done by a trial-and-error procedure. The extinction efficiencies for different models are shown in Figure 1. The adopted 10 μm peak absorption strength is $2200 \text{ cm}^2 \text{ g}^{-1}$.

We have adopted the interstellar grain size distribution (Mathis, Rumpel, & Norsieck 1977, hereafter MRN)

$$n(a)da = A_i a^{-\alpha} da, \quad (1)$$

where $A_i = 10^{-25.11} \text{ cm}^{2.5} H^{-1}$ for silicate grains (Draine & Lee 1984), a is the radius of dust grains, and $\alpha = 3.5$ for $0.005 \geq a \geq 0.25 \mu\text{m}$. Biermann & Harwit (1980) suggested that the same grain size distribution law also applied in the case of circumstellar grains. Griffin (1990) showed that varying grain size mainly affects the near-infrared fluxes but has little effect on the emergent fluxes in the mid- and far-infrared. Thus, we assume that the index of the grain size distribution remains constant.

Anticipating that the far-infrared observations are not well fitted by Draine & Lee's optical constants, we have assumed that the extinction efficiency follows a power law

$$Q(\text{ext}) \propto \lambda^{-p}, \quad (2)$$

where $p = 2$ for crystalline material and $p = 1$ for amorphous layer-lattice material (Tielens & Allamandola 1987).

2.3. Silicate Core-Ice Mantle Grains

Some late-type giants show a prominent absorption feature around 3 μm , attributed to the OH stretching mode in water-ice (Gillett & Forrest 1973; Merrill & Soifer 1974; Roche & Aitken 1984; Forville et al. 1987). These objects also show structure in their 10 μm silicate feature due to the H_2O libration mode. Close inspection of *IRAS* LRS spectra revealed that

some stars in our sample also exhibit a broad 10 μm feature, possibly due to the presence of water-ice. This ice is expected to condense onto silicate cores, forming a grain mantle when the latter has cooled to a temperature of about 150 K. Aannestad (1975) has studied the optical properties of silicate core-ice mantle grains which showed a very prominent absorption at 3.1 μm . However, the optical constants used were of crystalline material. Here, the calculation is made using the previously described silicate properties (§ 2.2) and amorphous ice optical constants (Leger et al. 1983). The radius of the coated grain, a_m , is given by

$$a_m = a_c + \Delta a, \quad (3)$$

where a_c is radius of the silicate core and Δa is the thickness of the ice mantle. In this case, the core size follows the MRN grain size distribution. For a grain mantle grown by accretion, the mantle thickness will be independent of the core size (Pendleton 1987), and we adopted $\Delta a = 0.007 \mu\text{m}$. This corresponds to all the elemental oxygen that is not in the form of silicates or CO. The calculation of $Q(\text{ext})$ for a coated sphere is given by Bohren & Huffman (1983). The far-infrared emissivity is assumed to follow a λ^{-3} law for $\lambda \geq 80 \mu\text{m}$ (Aannestad 1975). The adopted extinction curves for silicate core-ice mantle grains are shown in Figure 2.

2.4. Free Parameters

The following are parameters required as inputs in the radiative transfer calculations. The adopted values are listed in Table 1.

2.4.1. Stellar Parameters

Stellar parameters include stellar radius, effective temperature, and distance which are related to the stellar luminosity. Most of the stars are unresolved, and their actual sizes are not known. However, for stars with optically thin circum-

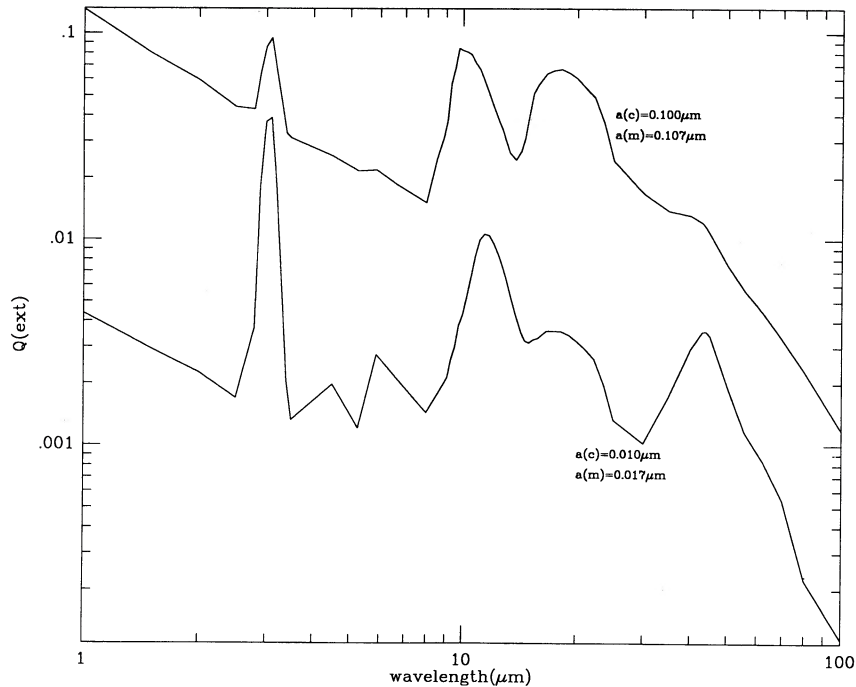


FIG. 2.—Extinction coefficients for silicate core-ice mantle grains for different core radius but with the same mantle thickness. For smaller a_c , ice features dominate (i.e., at 3, 12, and 46 μm), but for larger a_c , silicate features can clearly be seen.

stellar shells (i.e., 10 μm feature is in emission) it is assumed that the observed *IRAS* LRS flux at 8 μm is the stellar continuum. Therefore, fitting the energy distribution to this point yields the stellar radius. This also applies for stars with a self-reversed 10 μm feature. For optically thick shells, the 8 μm flux is dominated by dust emission, and we have reverted to the

normal assumption of a constant luminosity of $10^4 L_\odot$, using the appropriate effective temperature and distance (see below).

The effective temperature can be determined from optical spectra for optically thin stars. In most cases, it was obtained from near-infrared photometry (e.g., Hyland et al. 1972). For optically thick stars, however, the effective temperature is

TABLE 1
INPUT PARAMETERS FOR RADIATIVE TRANSFER CALCULATIONS

Sources	D (kpc)	T_* (K)	R_* (cm)	\dot{M}_d ($M_\odot \text{ yr}^{-1}$)	v_e (km s^{-1})	r_0 (cm)	$\tau_{9.7}$	p^a
AFGL 1822	1.80	2000	5.7E+13	2.6E-07	12.9	2.5E+14	6.29	1.0
AFGL 2199	1.60	1800	9.0E+13	1.8E-07	15.0	2.9E+14	3.24	1.0
AFGL 230	2.80	2000	1.4E+14	2.0E-06	12.7	7.8E+14	16.0	1.5
AFGL 2362	2.05	2000	5.5E+13	2.1E-07	17.9	2.2E+14	4.20	1.5
GX Mon	0.50	2500	4.0E+13	7.2E-09	17.5	2.5E+14	0.13	1.0
IRAS 16105-4205	0.80	2000	6.6E+13	4.6E-07	15.0	2.9E+14	5.68	1.0
IRC +10322	0.60	2000	4.8E+13	1.4E-08	15.0	1.9E+14	0.39	1.5
IRC +10523	1.10	2300	4.3E+13	4.0E-09	10.4	2.3E+14	0.13	1.0
IRC -20197	0.78	2250	4.2E+13	3.8E-08	12.0	2.1E+14	1.18	1.5
IRC +40004	1.10	2000	8.6E+13	9.0E-08	24.2	3.1E+14	0.96	1.0
IRC +50137	0.82	1850	3.9E+13	7.4E-08	14.7	1.3E+14	2.97	1.0
IRC +70066	0.80	2200	7.0E+13	2.8E-08	21.1	3.4E+14	0.31	1.5
OH 1.1-0.8	1.20	2000	6.5E+13	2.5E-07	19.5	2.6E+14	3.88	1.0
OH 26.5+0.6	0.98	2200	5.0E+13	1.2E-06	15.4	3.1E+14	19.6	1.0
OH 32.8-0.3	4.30	2000	7.6E+13	2.2E-06	17.7	4.2E+14	19.0	1.0
OH 343.4+1.3	3.50	2000	6.1E+13	8.0E-07	21.5	3.0E+14	9.71	1.0
OH 39.9-0.0	5.50	2000	5.5E+13	3.0E-07	14.6	2.3E+14	7.02	1.0
OH 44.8-2.3	2.41	2000	6.9E+13	2.8E-07	16.5	2.8E+14	4.85	1.5
OH 65.4+1.3	6.00	2000	6.4E+13	3.1E-07	17.0	2.6E+14	5.61	1.0
R Cas	0.216	2100	4.0E+13	1.9E-09	11.0	1.8E+14	0.08	1.0
R Hor	0.265	2500	3.5E+13	6.2E-10	7.0	2.2E+14	0.03	1.0
VX Sgr	1.70	2500	2.5E+14	8.8E-08	19.7	1.5E+15	0.24	1.0
WX Ser	0.72	1900	3.6E+13	9.0E-09	7.4	1.3E+14	0.74	1.5
Z Cyg	0.718	2500	2.0E+13	6.0E-10	2.3	1.3E+14	0.17	1.0

^a The far-infrared extinction efficiency is assumed to be given by $Q(\text{ext}) \propto \lambda^{-p}$.

somewhat arbitrarily assumed to be 2000 K, characteristic for the tip of the AGB. However, the emergent spectrum is now dominated by cool dust which is heated by the reradiated emission of warm dust closer in. As a result, the emergent spectrum is not very sensitive to the stellar temperature (Schutte & Tielens 1989).

The value adopted for the stellar luminosity (or equivalently, the distance) has no influence on the emergent spectrum as long as the total dust column density is kept constant (Jones & Merrill 1976; Bedijn 1977). However, it does set the size scale of the envelope. The uncertainties in the distance actually forms the main source of error in the determination of the envelope parameters (i.e., \dot{M}_d , R_*). This will be discussed in some detail in § 3.3.

Distances to many stars have been obtained from the published literature. Each author used different methods, but the most reliable one to date is "phase lag" (e.g., Herman & Habing 1985; Herman, Burger, & Pennix 1986). Others can be obtained from the period-OH luminosity relation (e.g., Nguyen-Q-Rieu et al. 1979) or from kinematic distance calculations. Some stars have their distances calculated by assuming luminosity of $10^4 L_\odot$ (e.g., Knapp & Morris 1985).

2.4.2. Wind Terminal Velocity

The terminal velocities are obtained from OH maser observations of OH/IR stars (Baud & Habing 1983; Bowers, Johnston, & Spencer 1983; Gehrz et al. 1985) and from CO outflow velocity (Knapp & Morris 1985). There is a slight difference between the velocity obtained from OH and CO observations on the order of 2 km s^{-1} (Heske et al. 1990). Here we assume that outflow velocity is the same as the terminal velocity of the dust and is constant throughout the shell.

2.4.3. Radius of Dust Shell

The inner radius of the dust shell, r_i , is taken to be where a grain first condenses out. For silicates, the condensation temperature, T_c , is 1000 K, that is, $r_i \propto T^{-4}$.

In the presence of dust, temperature is assumed to follow $r^2 \propto T^{-5}$. Hence the outer radius of the shell is determined by

$$\log(r_o) = -2.5 \log\left(\frac{T_o r_i^{-0.4}}{T_c}\right). \quad (4)$$

For this calculation, the temperature at the outer boundary, T_{out} , is taken to be 30 K. From the radiative transfer calculation, however, it is found that the temperature at this radius falls to 10 K for an optically thin envelope which is close to values for the interstellar medium. The exact location of the outer boundary has no influence on the emergent flux between 2 and $100 \mu\text{m}$.

2.4.4. Density Law

We assumed a constant mass-loss rate and a constant outflow velocity. This results in a r^{-2} dust density dependence. Other dust density distributions, that is, taking the acceleration near the inner radius into account, have been investigated by Schutte & Tielens (1989). However, this has little influence on the dust column density, as long as the dust column density is kept constant.

3. MODELS FOR INFRARED EMISSION

Detailed models for the infrared emission from circumstellar shells as a function of various free parameters have been produced by Jones & Merrill (1976), Bedijn (1977, 1987) and

Schutte & Tielens (1989). Here we concentrate on observed flux distribution of samples of AGB stars and deriving interesting physical parameters of the flow (i.e., the dust mass-loss rate).

The majority of stars in our sample was chosen from a list of OH/IR stars with known distances, OH outflow velocities and near-infrared photometry fluxes. Many of the stars have been observed in CO and therefore have their mass-loss rates estimated. However, the near-infrared fluxes were not obtained at the same epoch as the *IRAS* data, hence these will introduce uncertainty in mass-loss rate determined from detailed model fits. The variations in the near-infrared fluxes can be up to a factor of 2 (see, e.g., Evans & Beckwith 1977; Werner et al. 1980).

All the model fits are shown in Figure 3, and the derived parameters are listed in Table 1. Essentially, these fits yield the total $10 \mu\text{m}$ optical depth, $\tau(10)$, which can be translated into dust mass-loss rate using the derived inner radius of the dust shell, r_i , the outflow velocity, v_e , and the intrinsic strength of the $10 \mu\text{m}$ feature (Schutte & Tielens 1989)

$$\dot{M}_d \propto r_i v_e \frac{\tau(10 \mu\text{m})}{S(10 \mu\text{m})}. \quad (5)$$

The derived dust mass-loss rates are listed in Table 1.

3.1. Individual Sources

A few sources required special treatment in the modeling procedure.

3.1.1. AFGL 2199

This source was classified as a carbon star by Knapp et al. (1982). However, we found this source to exhibit a self-reversed silicate feature at $10 \mu\text{m}$ and silicate emission at $18 \mu\text{m}$.

3.1.2. OH 26.5+0.6

A further study has been made for OH 26.5+0.6 because of its optically thick nature. Evans & Beckwith (1977) observed the flux of this source which varied by almost 40% over a period of 1 yr. The observed 10 and $20 \mu\text{m}$ feature cannot be fitted by assuming the intrinsic $20:10 \mu\text{m}$ ratio to be 0.5 as in other cases. Also, the near-infrared opacity is much lower than in other stars. Clearly, a new set of optical constants is needed. This was done by scaling the $20:10 \mu\text{m}$ ratio to 0.8 and reducing the near-infrared extinction (Fig. 1). The overall fit to the infrared spectrum of this source is in Figure 3f. Figure 3g shows a detailed comparison with the LRS spectra of OH 26.5+0.6. The set of silicate dust properties used here produces a good fit to the detailed spectrum.

3.1.3. AFGL 230 = OH 127.8-0.0

This source has an extremely thick circumstellar shell. Heske et al. (1990) reported its distance of 2.8 kpc; hence this makes it a very luminous source ($L_* \sim 5 \times 10^4 L_\odot$). Again, the intrinsic $20:10 \mu\text{m}$ ratio for this source is found to be 0.8. A close inspection of Figure 3g reveals that AFGL 230 may have ice present since the $10 \mu\text{m}$ feature appears too broad to be explained by silicate absorption alone.

3.1.4. IRAS 16105-4205 and OH 32.8-0.3

These two sources show evidence for ice grains (de Muizon, d'Hendecourt, & Perrier 1986, Roche & Aitken 1984). Both were modeled with silicate core-ice mantle grains as described in § 2. The result is a much broader $10 \mu\text{m}$ feature (Fig. 3g). Also seen are a deep absorption feature at $3 \mu\text{m}$ and an emis-

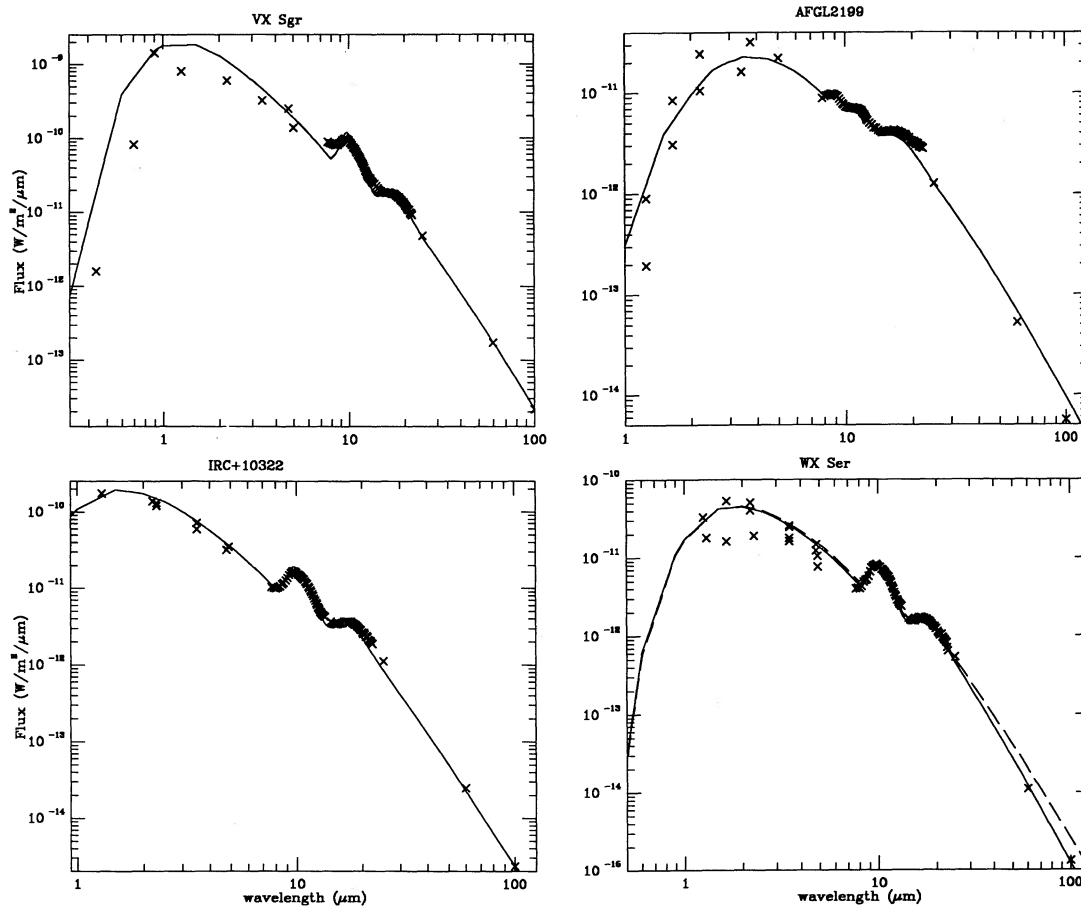


FIG. 3.—Detailed model fits (solid lines) of observed (crosses) infrared energy distributions of 24 stars. Parameters for each model are summarized in Table 1. Figs. 3a–3g show overall fit from $\lambda \leq 1$ to $100 \mu\text{m}$. The solid line for WX Ser in Fig. 3a is the best fit with $Q(\text{ext}) \propto \lambda^{-1.5}$, and the dashed line corresponds to $Q(\text{ext}) \propto \lambda^{-1.0}$. Fig. 3f shows a detailed fit of *IRAS* LRS spectra of four stars discussed in the text. NIR data have been taken from Lockwood (1970); Simon et al. (1972); Wilson et al. (1972); Dyck & Lockwood (1974); Strecker & Ney (1974); Lebofsky et al. (1976); Merrill & Stein (1976); Thomas et al. (1976); Evans & Beckwith (1977); Werner et al. (1980); Jones et al. (1983); Fix & Mutel (1984); and Baud et al. (1985).

sion feature at $50 \mu\text{m}$ (Fig. 3f). The model slightly underestimated the depth of the $3 \mu\text{m}$ feature. However, LRS spectra and $3 \mu\text{m}$ spectra of OH 32.8–0.3 (T. R. Geballe 1990, private communication) were not obtained at the same epoch, so slight variation in strengths of the two features might be expected. Unfortunately, there is no photometric information on *IRAS* 16105–4205 which can be used to scale the published $3 \mu\text{m}$ data by de Muizon et al. (1986) to the LRS spectra. The long-wavelength lattice vibrations of water-ice ($\sim 46 \mu\text{m}$) are not very apparent in the calculated spectra of these sources. Much larger mass-loss rates are required to get appreciable optical depth in these modes.

3.2. Dust Properties

From modeling 24 sources, the index of the far-infrared emissivity, p , is found to be between 1 and 1.5. This implies that grains formed in the circumstellar environment are amorphous rather than crystalline and have a layer-lattice structure (Tielens & Allamandola 1987). Sources with $p = 1.0$ have dust opacity at $60 \mu\text{m}$ of $240 \text{ cm}^2 \text{ g}^{-1}$, as assumed by Herman et al. (1986), and sources with $p = 1.5$ have dust opacity of $160 \text{ cm}^2 \text{ g}^{-1}$, as assumed by Jura (1987).

For most sources with silicate emission, the 20:10 μm ratio is fairly constant, that is, ~ 0.5 . This ratio also holds for sources with self-reversed 10 μm features. However, for very optically

thick stars where 10 μm is now in total absorption, this ratio increases to about 0.8 (see §§ 3.1.1 and 3.1.2). Possibly, this is a consequence of the temperature dependence of the optical properties of circumstellar silicate grains (Bedijn 1987). Some laboratory studies have shown that the 20:10 μm ratio increases with decreasing temperature (Day 1976). Thus, the cool dust prominent in heavily obscured sources may have, on average, an intrinsically higher 20:10 μm ratio than the warmer dust observed in optically thin sources.

3.3. Uncertainties in the Derived Parameters

As can be seen from equation (5), the uncertainty in the dust mass-loss rate is most affected by uncertainty in the size scale of the envelope (i.e., the inner radius, r_i) since the outflow velocity for these sources are known from the CO or OH observations and the optical depth can be deduced from the *IRAS* LRS spectra. The inner radius is calculated by assuming that the grains form where the temperature equals the condensation temperature of silicates. Apart from the actual condensation temperature selected, this will be affected by the radiation field of the star which, in turn, depends on the assumed stellar luminosity, L , and the chosen value of the condensation temperature.

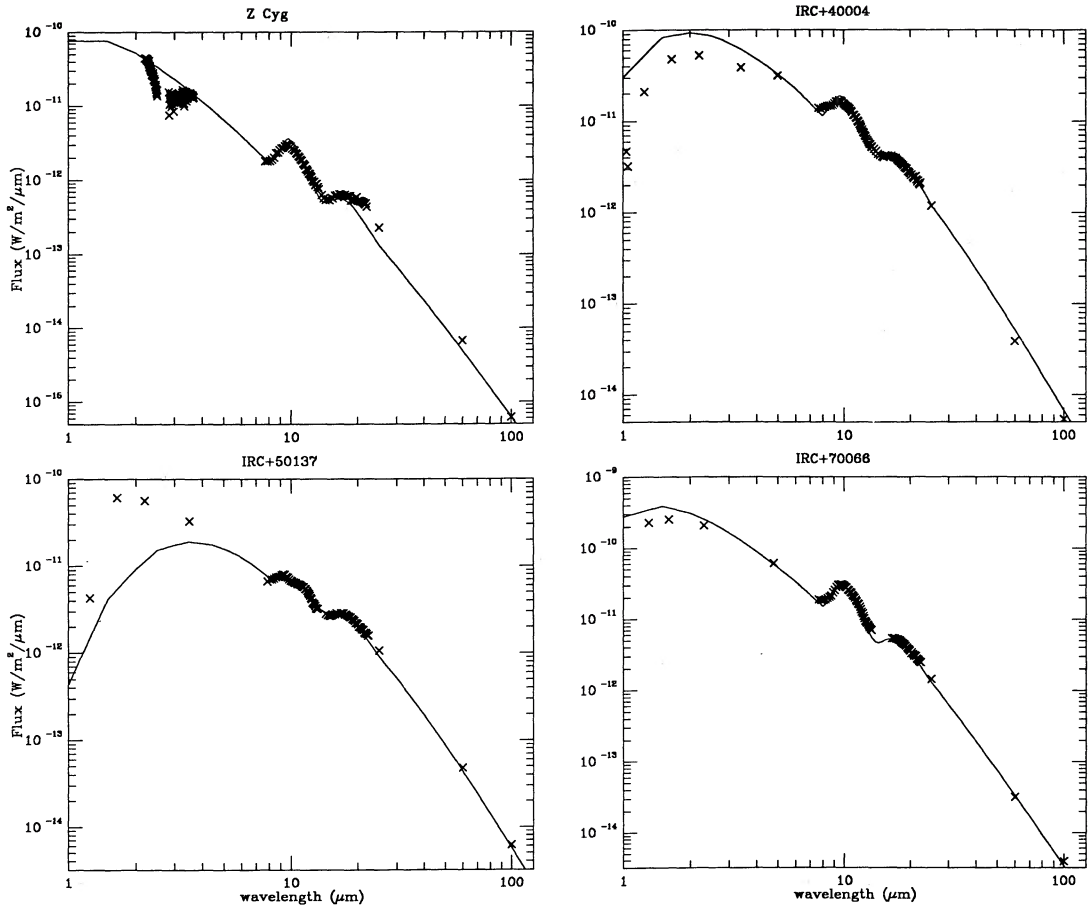


FIG. 3b

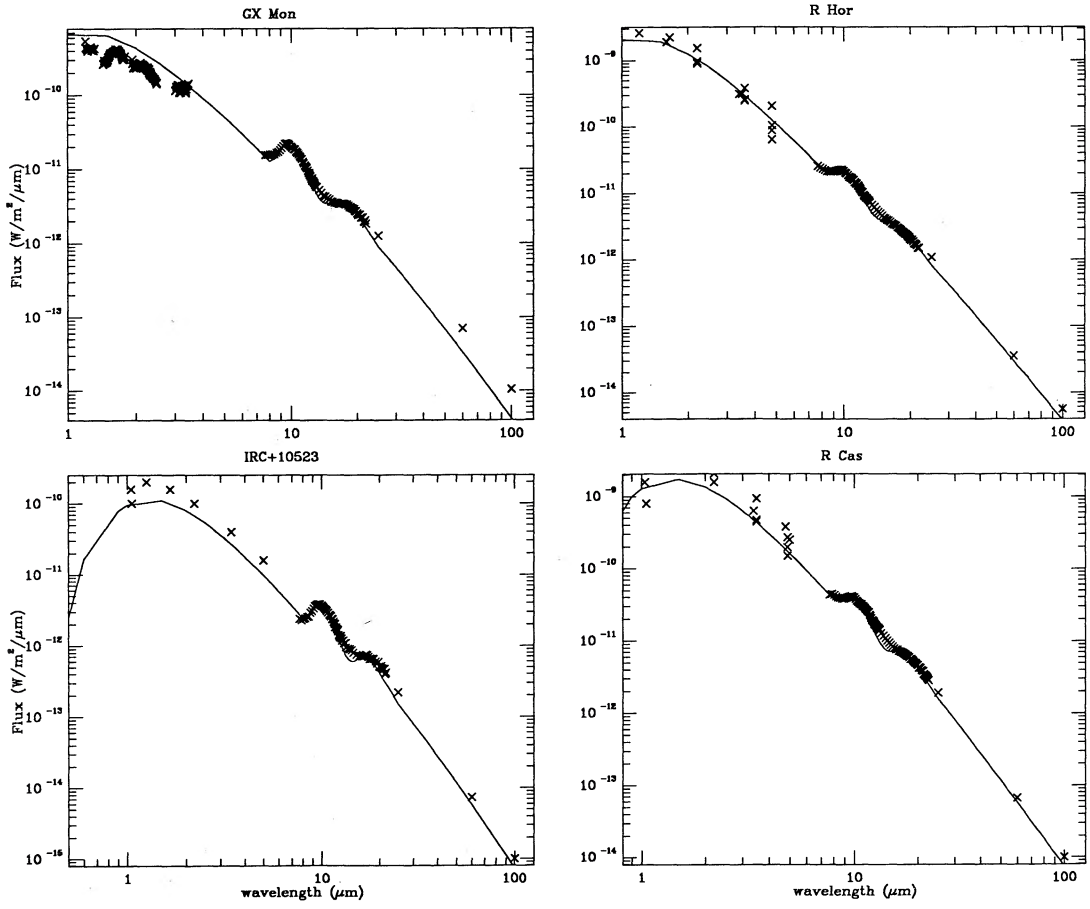


FIG. 3c

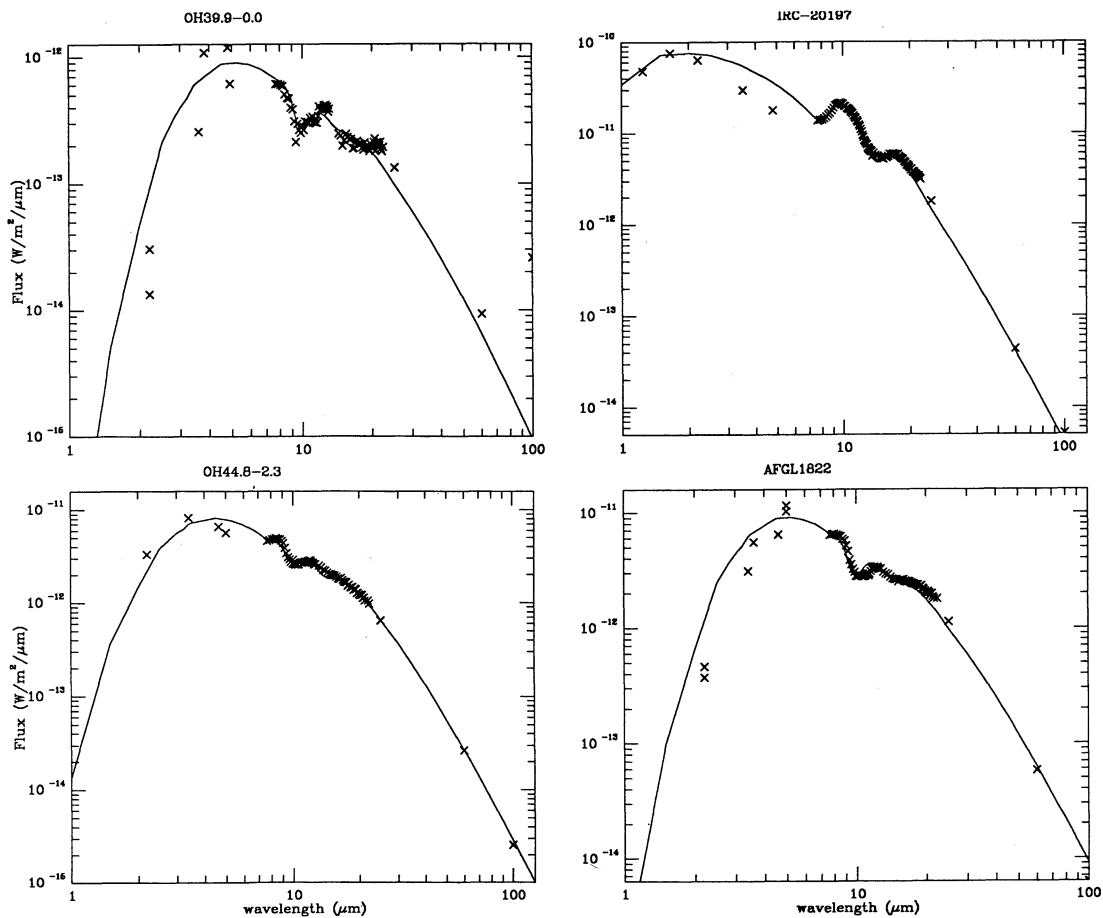


FIG. 3d

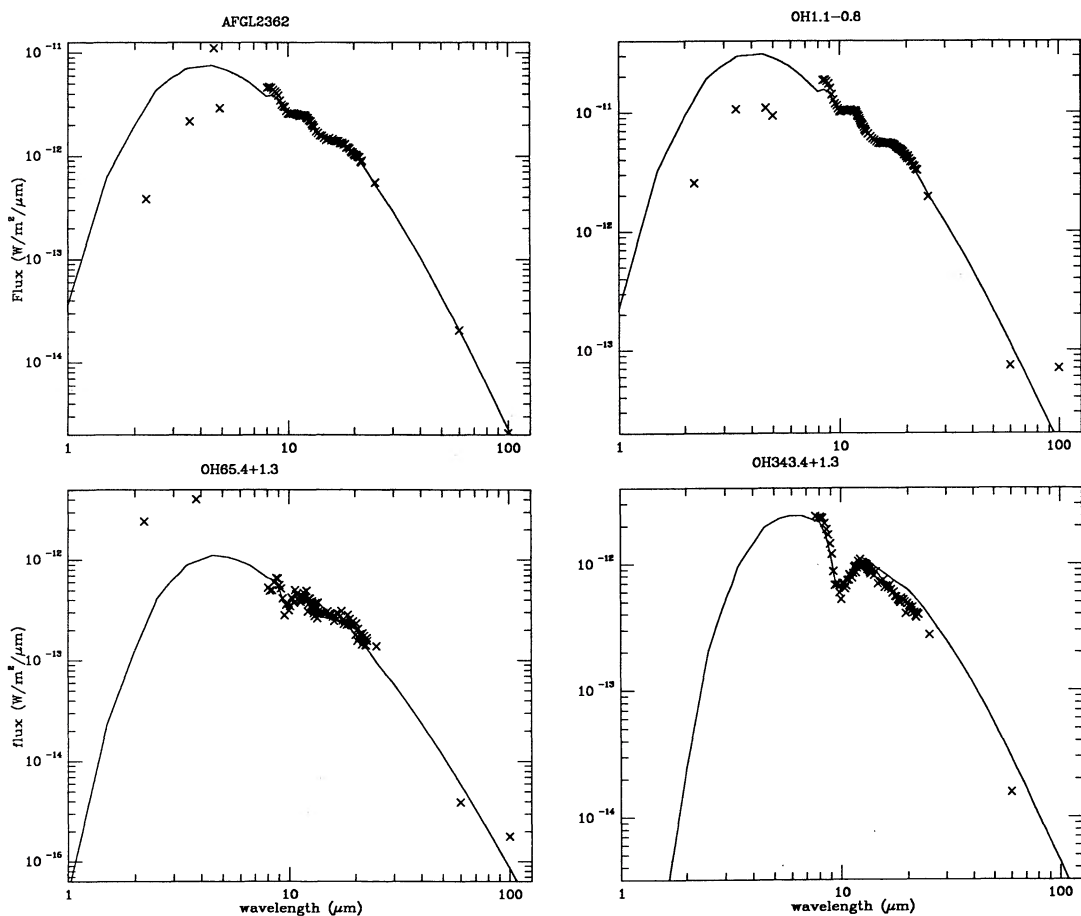


FIG. 3e

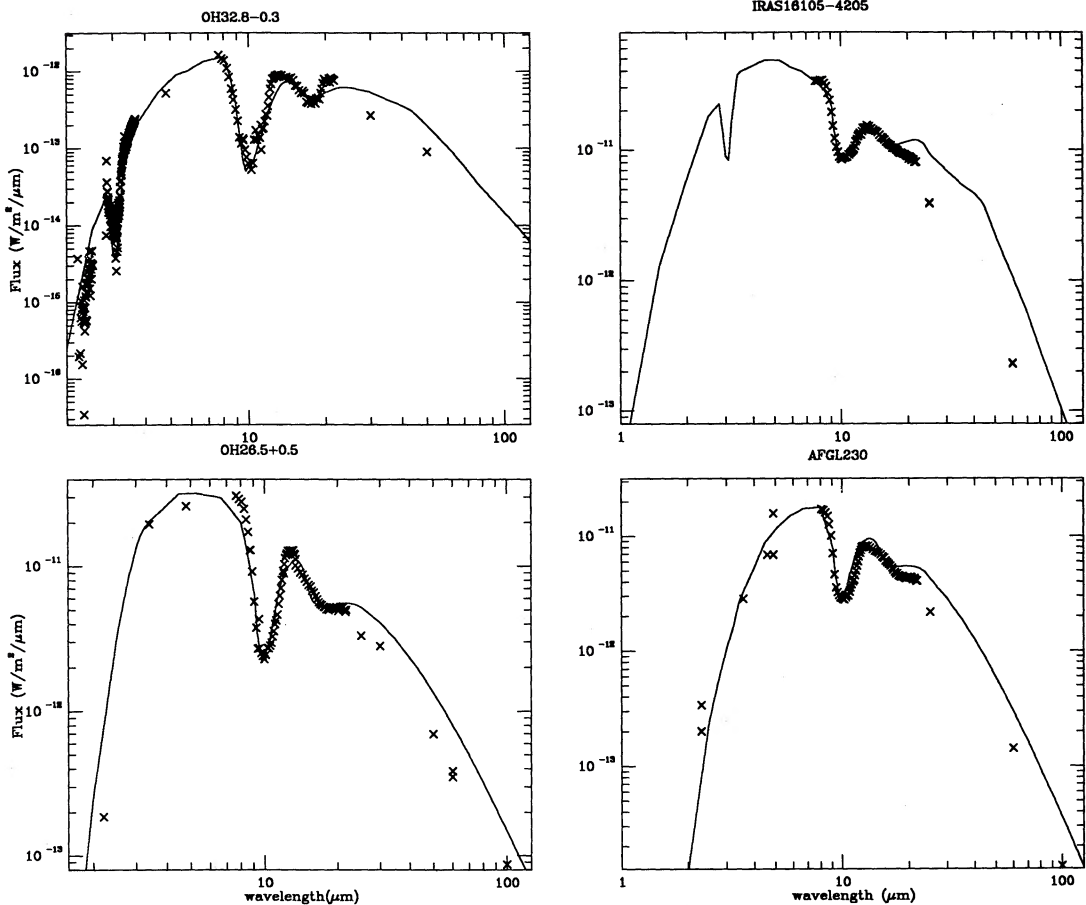


FIG. 3f

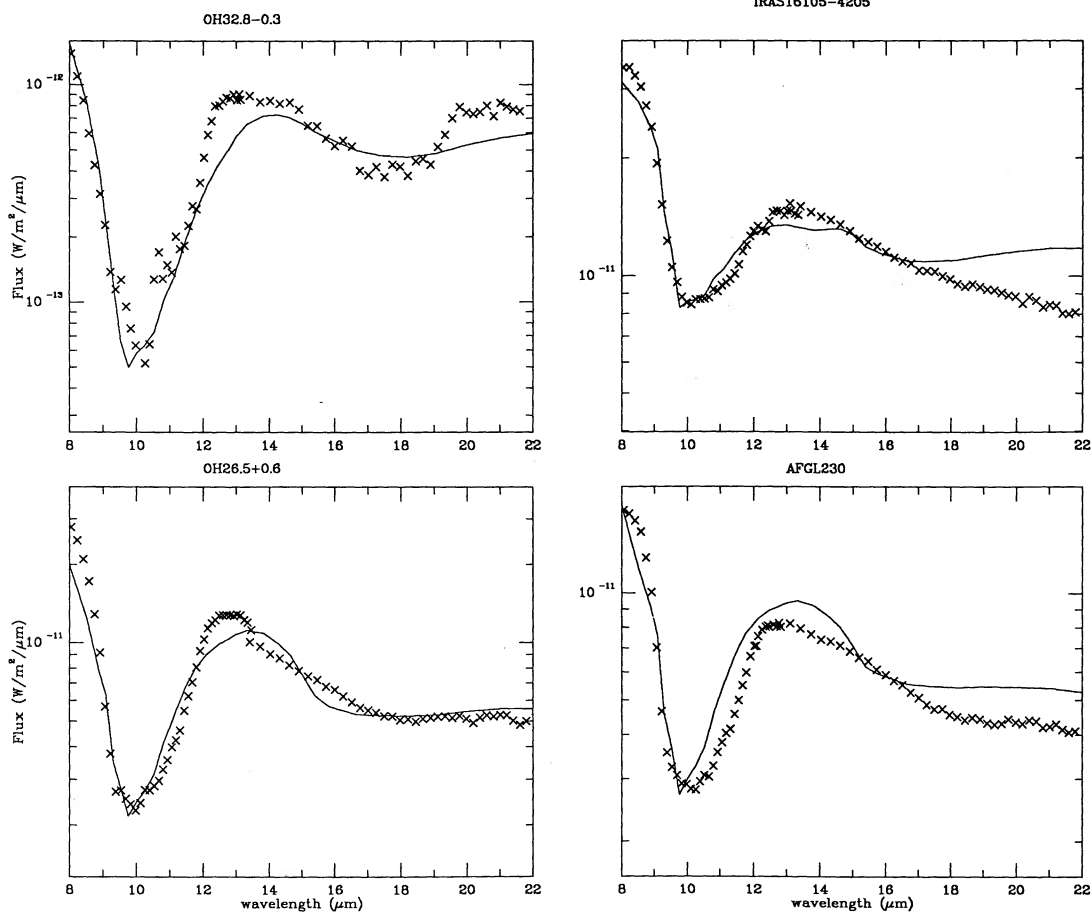


FIG. 3g

However, as noted by Schutte & Tielens (1989), variations in the adopted value for T_c are partially compensated for by variations in r_i required to fit the observed spectrum. The uncertainty in the derived mass-loss rate from T_c alone is therefore small (15%). For optically thin shells, the stellar radiation field is directly determined from the observed near-infrared and 8 μm fluxes, using the estimated distance, D . That is, r_i scales with $L^{0.5}$, and L depends only on D . The main uncertainty in the derived mass-loss rate, inner radius, and stellar radius results then from the adopted distance. For optically thick shells, the dust at the inner radius is heated by reradiated infrared emission from the dust shell itself, and the stellar parameters are of little importance. Consequently, they are not well constrained. The dust radiation field at the inner boundary is well determined from the fitting procedure. Thus, again, the main uncertainty in the derived mass-loss rate results from the uncertainty in the adopted distance. The most accurate distance determinations come from OH maser measurements (the phase lag method; Herman et al. 1986). This method is good to within a factor of 2, implying a similar uncertainty in r_i and hence \dot{M}_d .

4. COMPARISONS OF MASS-LOSS RATES

There are various methods for the determination of mass-loss rates which have been widely accepted. However, each has a certain degree of uncertainty. In this section, these will be compared to the dust mass-loss rates obtained from the detailed model fits (see Table 2).

4.1. Dust Mass-Loss Rates

Van der Veen & Habing (1988) derived a relationship between the ratio of 25 and 12 μm IRAS photometry fluxes and the observed mass-loss rate (from CO and OH observation)

$$\dot{M}_{25/12} = \frac{AL(F_{25}/F_{12})^\alpha}{v_{15}}, \quad (6)$$

where $\dot{M}_{25/12}$ is in $M_\odot \text{ yr}^{-1}$; L is in $10^4 L_\odot$, and v_{15} is in unit of 15 km s^{-1} $A = 7 \times 10^{-6}$, and $\alpha = 3$. Essentially, this relation equates the momentum in the outflow with the momentum of the absorbed photons (Salpeter 1974),

$$\dot{M}v = \tau_d L/c, \quad (7)$$

and replaces the dust optical depth in the above equation with the F_{25}/F_{12} ratio. This relationship is compared in Figure 4, with mass-loss rates derived from our detailed model fits, assuming a dust-to-gas ratio of 4×10^{-3} .

In order to theoretically underpin this relationship, a set of models was constructed with the same input parameters, but increasing mass-loss rate. The results are shown in Figure 4 as the solid curve. The calculated relation shows a concave curvature reflecting the shift of the peak of the Planck function through the IRAS 12 and 25 μm filters with increasing mass-loss rate, that is, cooler dust temperatures. Nevertheless, except for an offset in the dust-to-gas ratio, equation (6) gives a reasonable estimate of the mass-loss rate. The best fit to our results for dust mass-loss rates is given by $A = 1.8 \times 10^{-7}$, $\alpha = 4.96$ for $F_{25}/F_{12} < 0.85$, and $A = 1.2 \times 10^{-7}$, $\alpha = 2.37$ for $F_{25}/F_{12} > 0.85$. The corresponding relation for the gas mass-loss rate will depend on the assumed dust-to-gas ratio.

TABLE 2
MASS-LOSS ESTIMATES FROM VARIOUS METHODS

SOURCES	\dot{M}_{gas}		\dot{M}_{dust}		
	\dot{M}_{CO}	\dot{M}_{OH}	$\dot{M}_{F_{25}/F_{12}}$	$\dot{M}_{60\mu\text{m}}$	\dot{M}_d
AFGL 1822	...	1.5E-05	5.9E-07	3.0E-07	2.6E-07
AFGL 2199	1.3E-05	...	2.1E-07	1.9E-07	1.8E-07
AFGL 230	1.1E-05	2.9E-05	2.2E-06	1.2E-06	2.0E-06
AFGL 2362	2.5E-05	8.0E-06	1.4E-07	3.0E-07	2.1E-07
GX Mon	1.5E-06	3.3E-06	1.3E-08	3.7E-08	7.2E-09
IRAS 16105-4205	8.1E-06	...	2.7E-07	2.7E-07 ^a	4.6E-07
IRC + 10322	3.4E-06	5.1E-07	1.8E-08	3.1E-08	1.4E-08
IRC + 10523	...	8.2E-07	1.4E-08	1.2E-08	4.0E-09
IRC - 20197	1.8E-06	4.3E-06	7.1E-08	6.5E-08	3.8E-08
IRC + 40004	3.2E-05	...	2.8E-08	1.0E-07	9.0E-08
IRC + 50137	6.5E-06	5.8E-06	6.1E-08	1.0E-07	7.4E-08
IRC + 70066	9.0E-06	...	9.9E-09	5.5E-08	2.8E-08
OH 1.1-0.8	...	2.2E-05	1.5E-07	2.2E-07	2.5E-07
OH 26.5+0.6	4.6E-05	4.8E-05	4.7E-07	3.8E-07	1.2E-06
OH 32.8-0.3	2.8E-05	6.7E-05	1.9E-06	1.0E-05 ^a	2.2E-06
OH 343.4+1.3	...	3.9E-05	2.5E-07	4.9E-07	4.9E-07
OH 39.9-0.0	...	4.5E-05	4.8E-07	5.6E-07	3.0E-07
OH 44.8-2.3	2.2E-05	2.0E-05	2.4E-07	4.3E-07	2.8E-07
OH 65.4+1.3	...	3.5E-05	3.5E-07	2.6E-07	3.1E-07
R Cas	7.0E-07	7.5E-07	1.8E-09	5.3E-09 ^b	1.9E-09
R Hor	...	7.2E-07	5.4E-09 ^c	2.1E-09 ^b	6.2E-10
VX Sgr	...	3.8E-05	2.1E-07	2.0E-07	8.8E-08
WX Ser	2.2E-07	1.4E-06	1.3E-08	1.3E-08	9.0E-09
Z Cyg	...	4.2E-07	1.4E-07 ^c	2.1E-09	6.0E-10

^a 60 μm flux is dominated by ice emission. Dust mass-loss rate determined from 60 μm flux is unreliable.

^b 60 μm flux is dominated by the star. Dust mass-loss rate determined from the 60 μm flux is unreliable.

^c Dust and gas are not well coupled in these objects. Dust mass-loss rate determined from this method is unreliable.

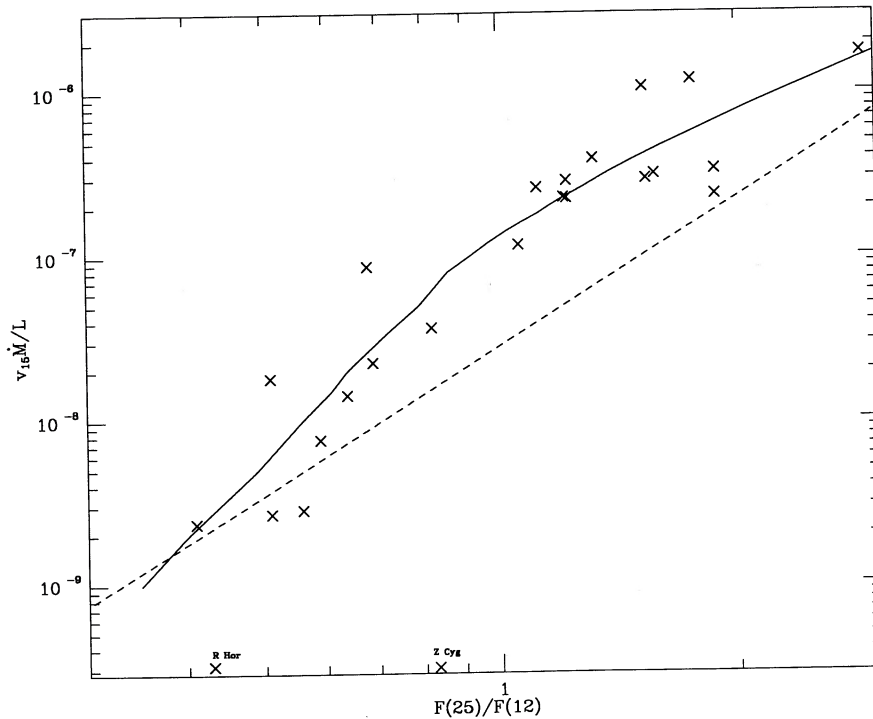


FIG. 4.—Dust mass-loss rates obtained from modeling, corrected for velocity and luminosity, as a function of ratio of fluxes at 25 and 12 μm . Solid line is from the same size stars with increasing mass-loss rates. Dashed line is calculated from eq. (6).

The source Z Cyg and, to a lesser extent, R Hor form an exception to the general relationship displayed in Figure 4, reflecting their extremely low outflow velocity (Table 1). Apparently, this results from a breakdown in equation (7) for these objects, as illustrated in Figure 5. Possibly, the dust and gas do not couple well with each other in objects with such low

outflow velocities as Z Cyg and R Hor (i.e., large dust drift velocity). In view of the general low outflow velocity ($\leq 4 \text{ km s}^{-1}$) of “short” period Miras ($P \leq 400$ days; Sivagnanam et al. 1989), this may form a common problem for such objects, and the use of equation (6) in deriving their mass-loss rate should be discouraged.

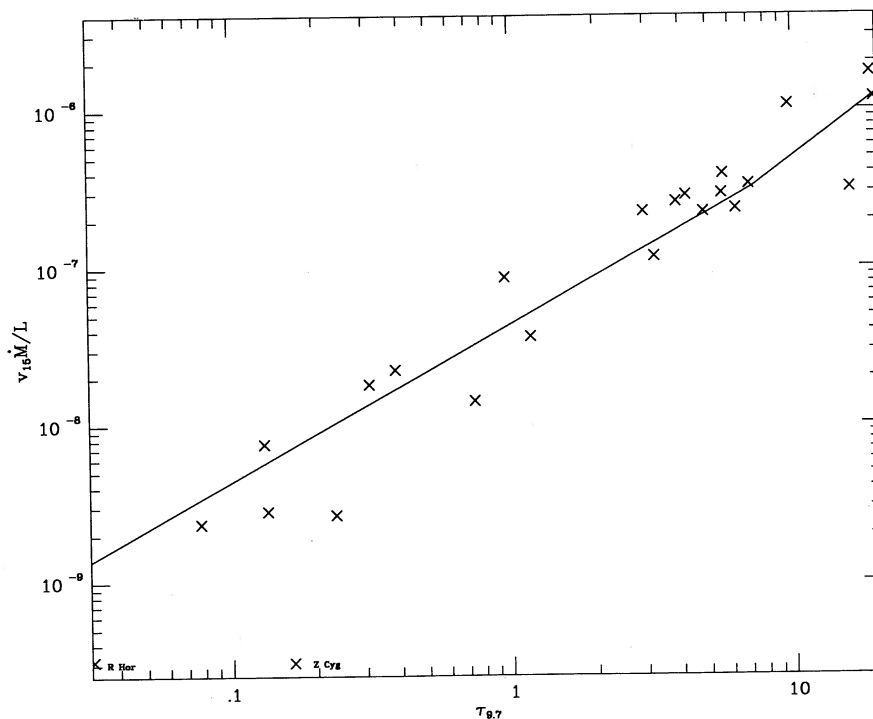


FIG. 5.—A plot of mass-loss rate, corrected for velocity and luminosity, as a function of 9.7 μm optical depth. The solid line is from the running models with increasing mass-loss rates. The relationship is expected to follow a straight line with a slope of $1/c$ for radiatively driven wind.

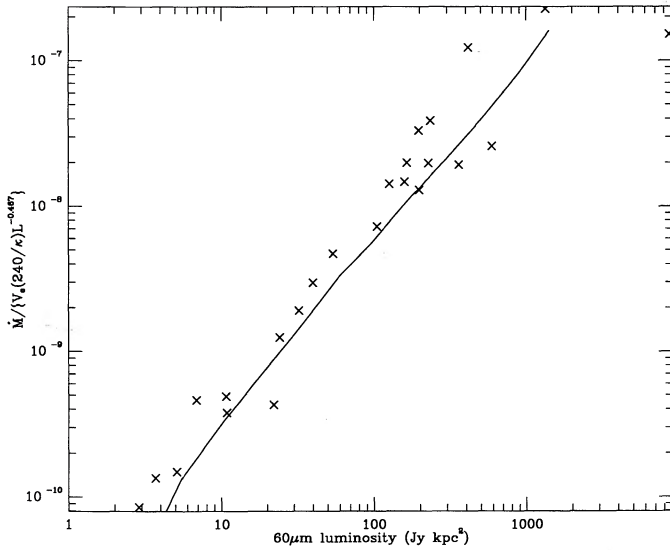


FIG. 6.—Comparison of dust mass-loss rates obtained from infrared modeling, corrected for expansion velocity, dust opacity, and luminosity, as a function of $60\ \mu\text{m}$ luminosity. The solid line is for models of the same stars but with increasing mass-loss rates.

IRAS $60\ \mu\text{m}$ photometry values have also been used to estimate mass-loss rates. Assuming the circumstellar shell is optically thin at long wavelengths, Herman et al. (1986) derived the relationship between the $60\ \mu\text{m}$ flux and the dust mass-loss rate as

$$\dot{M}_{60\mu\text{m}} = \eta_{60} F_{60} D^2 L^{-0.467} v_e \frac{240.0}{\kappa}, \quad (8)$$

where $\dot{M}_{60\mu\text{m}}$ is in $M_{\odot}\ \text{yr}^{-1}$, $\eta_{60} = 4.397 \times 10^{-11}$, F_{60} is the *IRAS* $60\ \mu\text{m}$ flux in Jy using a power-law color correction (*IRAS* Explanatory Supplement 1988), D is the distance in kpc, L is the luminosity in $10^4 L_{\odot}$, and v_e is the expansion velocity in km s^{-1} , and κ is the dust opacity at $60\ \mu\text{m}$.

Figure 6 compares the mass-loss rates determined from our detailed model fits with the $60\ \mu\text{m}$ luminosity. These mass-loss rates have been scaled by the appropriate outflow velocity, stellar luminosity, and $60\ \mu\text{m}$ dust opacity. For the latter, recall that all stars with a far-infrared index, p , of 1.0 and 1.5 have $60\ \mu\text{m}$ opacity of 240 and $160\ \text{cm}^2\ \text{g}^{-1}$, respectively. In general, there is a tight relationship between dust mass-loss rate and $60\ \mu\text{m}$ luminosity. However, this relationship is somewhat steeper than indicated by equation (8). Essentially, this reflects the breakdown of the optically thin approximation, which forms the basis of the above equation. The solid line in Figure 6 represents the results of a series of models in which the total dust column density was varied. It follows the mass-loss rate determined by our detailed model fits very well. The scatter represents the accuracy of those model fits to the observed $60\ \mu\text{m}$ flux. A better representation of the relation is

$$\dot{M}_{60} = \eta_{60,\text{new}} (F_{60} D^2)^{1.26} L^{-0.467} v_e \frac{240.0}{\kappa}, \quad (9)$$

where $\eta_{60,\text{new}} = 1.0 \times 10^{-10}$. The derived dust mass-loss rates from detailed model fits and those directly derived from the *IRAS* $60\ \mu\text{m}$ fluxes using a new constant are in good agreement when the appropriate $60\ \mu\text{m}$ dust opacity is taken into account. Figure 6 shows a turnover point for the very low dust mass-

loss rates. By extrapolation of the model (solid) curve, it is found that $60\ \mu\text{m}$ luminosity becomes a constant, which is expected since this is the stellar contribution, unattenuated by dust.

4.2. Gas Mass-Loss Rates

The mass-loss rate can also be determined from OH maser observations. These have shown that the OH maser is saturated and radiatively pumped (Harvey et al. 1974). Pumping is done by $35\ \mu\text{m}$ photons emitted by dust in the outflow (Elitzur et al. 1976). The OH maser luminosity is proportional to the pump rate, that is the $35\ \mu\text{m}$ luminosity. Since the latter depends mainly on the dust mass-loss rate, the OH luminosity should be well correlated with the dust mass-loss rate. Such correlation is well supported by airborne and space-based observations (Werner et al. 1980; Herman & Habing 1985; Herman et al. 1986; Sivagnanam et al. 1989). The relation to the mass-loss rate, however, is less well established.

The observed OH luminosity and the $35\ \mu\text{m}$ luminosity, derived from our model fits to the *IRAS* observations ($F_{35} D^2$) are compared to the dust mass-loss rate in Figure 7. There is clearly a good correlation over three orders of magnitude. The scatter in the $35\ \mu\text{m}$ luminosity merely reflects the "goodness" of our model fits to the far-infrared data. The much larger scattering in the OH luminosity correlation may represent temporal variations which can be as large as a factor of 2. The derived efficiency of the OH maser pump is about 0.3 for the higher mass-loss rate and seems to decrease with the mass-loss rate (see also Herman et al. 1986). From our models, we derive the following relation between the dust mass-loss rate and the OH luminosity, assuming dust-to-gas ratio of 5×10^{-3} :

$$\dot{M}_{\text{OH}} = 1.86 \times 10^{-7} L_{\text{OH}}^{0.78} v_e \frac{1.6 \times 10^{-4}}{f_{\text{OH}}}, \quad (10)$$

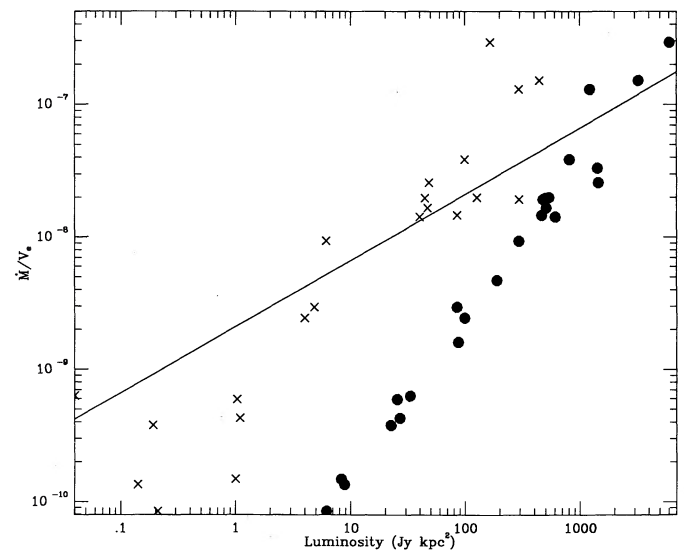


FIG. 7.—A plot of mass-loss rate corrected for velocity as a function of OH (crosses) and $35\ \mu\text{m}$ (solid) luminosity. The solid line is mass-loss rate given by the Baud & Habing relation, assuming dust-to-gas ratio of 5×10^{-3} . For the OH mass-loss rate, OH abundance is assumed to be 1.6×10^{-4} (cf. eq. [11]). The mass-loss rates are derived from $35\ \mu\text{m}$ luminosity, L is assumed to be 10^4 , and κ_{35} is assumed to be 418 (cf. eq. [8]). Values of OH fluxes were taken from Epchtein et al. (1980); Baud & Habing (1983); te Lintel Hekkert et al. (1989); and van der Veen & Rutgers (1989).

where L_{OH} is the OH luminosity in Jy kpc², v_e is the outflow velocity in km s⁻¹, and f_{OH} is the OH abundance, in this case, assumed to be 1.6×10^{-4} . This is considerably different from the relation derived by Baud & Habing (1983). They noted empirically that OH masers have approximately constant surface brightness and assumed that the OH column density is constant and equal to the minimum value required for saturation [i.e., $N(\text{OH}) = 10^{17}$ cm⁻², corresponding to $N(\text{H}_2) = 6 \times 10^{20}$ cm⁻²]. Theoretically, the OH column density is set by penetration depth of ambient UV photons and is approximately constant over the relevant parameter space (Huggins & Glassgold 1982; Netzer & Knapp 1987). Using these two relations and assuming a constant mass-loss rate, Baud & Habing (1983) derived the following expression for the gas mass-loss rate:

$$\dot{M}_{\text{OH}} = 4.2 \times 10^{-7} v_e S_{\text{OH}}^{0.5} D \frac{1.6 \times 10^{-4}}{f_{\text{OH}}}, \quad (11)$$

where S_{OH} is the geometric mean flux of the two OH peaks in Jy and D is distance in kpc. This relation is also shown in Figure 7, assuming a dust-to-gas ratio of 5×10^{-3} . The discrepancy between these two mass-loss rate determinations was noted before and (indirectly) ascribed to the variations in the dust-to-gas ratio (Herman et al. 1986). From our results, this would imply that the ratio varies from 0.001 for optically visible Miras to 0.07 for heavily obscured OH/IR stars. The latter is actually much larger than expected for silicate condensation in gas with solar elemental composition (~ 0.006 for MgFeSiO₄). Possibly, this is related to the onset of the superwind at the tip of the AGB. The dust mass-loss rates determined from the infrared refer to the inner ($\sim 3 \times 10^{14}$ cm) part of the envelope where most of the opacity occurs. In contrast, the OH maser is located around a few 10^{16} cm. Thus, while the OH measures material ejected about 2×10^3 yr ago, the infrared pertains to more recent ($< 10^2$ yr) ejecta.

Mass-loss rates from CO observations are taken from Knapp & Morris (1985) who observed stars in CO ($J = 1-0$) transition. The mass-loss rate for a star with optically thick CO line profile is given by

$$\dot{M}_{\text{CO}} = 5 \times 10^{-14} T_A v_{\text{CO}}^2 f_{\text{CO}}^{0.85} D^2 \theta^2, \quad (12)$$

where \dot{M}_{CO} is in M_{\odot} yr⁻¹, T_A is the antenna temperature in K, v_{CO} is the CO outflow velocity in km s⁻¹, f_{CO} is the CO abundance, D is the distance in kpc, and θ is half-power beamwidth of the telescope in arcseconds. For oxygen-rich stars, a CO abundance of 3×10^{-4} is appropriate.

CO mass-loss rates, scaled to the appropriate distance and velocities, are compared to the dust mass-loss rates in Figure 8. While for stars with low mass-loss rates (i.e., Miras), the two are in agreement with a dust-to-gas ratio of 0.003, a much larger ratio (0.08–0.2) is obtained for optically thick OH/IR stars. This is not physically realistic, and instead we attribute this discrepancy to the extremely low CO excitation tem-

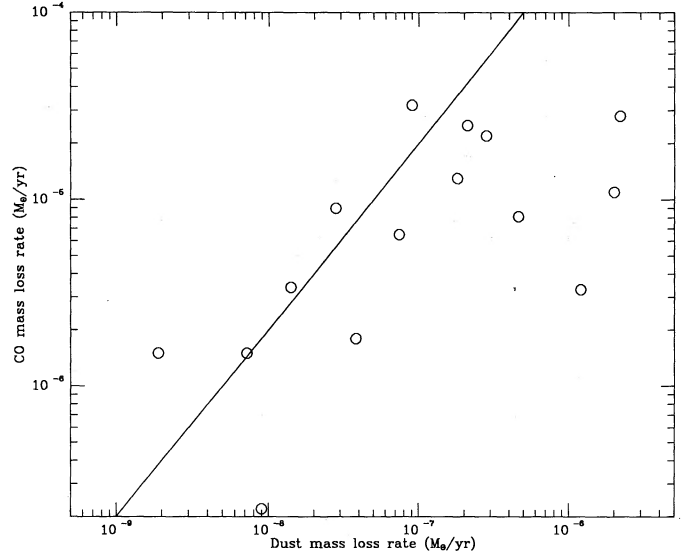


FIG. 8.—Comparison of CO and dust mass-loss rates. Solid line is for constant dust-to-gas ratio of 5×10^{-3} .

perature expected in such envelopes (Heske et al. 1990) and the consequent breakdown of equation (12). As for OH, the CO emission originates from far out in the envelope. Thus some of the difference between the derived dust and CO mass-loss rates may indicate evolution of the mass-loss rate (Baud & Habing 1983).

5. CONCLUSION

In this paper, 24 OH/IR stars have been chosen for infrared modeling of the energy distribution using *IRAS* LRS spectra. A set of silicate optical constants adapted from literature was used as an input parameter for radiative transfer calculation. The sources chosen range from those with emission to ones with deep absorption at $10 \mu\text{m}$. Dust mass-loss rates have been obtained for 24 stars. These have then been compared to values calculated from the *IRAS* $60 \mu\text{m}$ flux and the ratio of fluxes at 25 and $12 \mu\text{m}$. They agree to within a factor of 2 with the former, but there is a larger deviation with the latter.

A few sources with ice in their circumstellar envelopes have been modeled quite successfully with two-component dust of silicate core-ice mantle and silicate grains.

Comparison between CO and OH mass-loss rates with those calculated in this paper gives a wide range of values, and it is suggested that the dust-to-gas ratio is not constant for all OH/IR stars.

Studies on “The Nature of Interstellar Dust” at NASA Ames are supported by grant 399-500-0005 under the Long Term Space Astrophysics program.

REFERENCES

- Aannestad, P. A. 1975, *ApJ*, 200, 30
 Baud, B., & Habing, H. J. 1983, *A&A*, 127, 73
 Baud, B., Habing, H. J., Matthews, H. E., & Winnberg, A. 1979, *A&AS*, 35, 179
 Baud, B., Sargent, A. L., Werner, M. W., & Bentley, A. F. 1985, *ApJ*, 292, 628
 Bedijn, P. J. 1977, Ph.D. thesis, Rijksuniversiteit Leiden
 ———. 1987, *A&A*, 186, 136
 Biermann, P., & Harwit, M. 1980, *ApJ*, 241, L107
 Bohren, C. F., & Huffman, D. R. 1983, *Absorption and Scattering of Light by Small Particles* (New York: John Wiley)
 Bowers, P. F. 1978, *A&A*, 64, 307
 Bowers, P. F., Johnston, K. J., & Spencer, J. H. 1983, *ApJ*, 274, 733
 Day, K. L. 1976, *ApJ*, 203, L99
 de Jong, T. 1983, *ApJ*, 274, 252
 de Muizon, M., d'Hendecourt, L. B., & Perrier, C. 1986, *Proc. 1st IRAS Conference, Light on Dark Matter*, ed. F. P. Israel (Dordrecht: Reidel), 221
 Draine, B. T., & Lee, H. M. 1984, *ApJ*, 285, 89
 Dyck, H. M., & Lockwood, G. W. 1974, *ApJ*, 189, 89
 Elituz, M., Goldreich, P., & Scoville, N. 1976, *ApJ*, 105, 384

- Epchtein, N., Guibert, J., Nguyen-Q-Rieu, Turon, P., & Wamsteker, W. 1980, *A&A*, 85, L1
- Evans, N. J., & Beckwith, S. 1977, *ApJ*, 217, 40
- Fix, J. D., & Mutel, R. L. 1984, *AJ*, 89, 406
- Forveille, T., Morris, M., Omont, A., & Likkell, L. 1987, *A&A*, 176, L13
- Gehrz, R. D., Kleinmann, S. G., Mason, S., Hackwell, J. A., & Grasdalen, G. L. 1985, *ApJ*, 290, 296
- Gillett, F. C., & Forrest, W. J. 1973, *ApJ*, 179, 483
- Griffin, I. P. 1990, *MNRAS*, 247, 591
- Haisch, B. M. 1979, *A&A*, 72, 161
- Harvey, P. M., Bechis, K. T., Wilson, W. J., & Ball, J. A. 1974, *ApJS*, 27, 311
- Herman, J., Burger, J. H., & Pennix, W. X. 1986, *A&A*, 167, 247
- Herman, J., & Habing, H. J. 1985, *Phys. Rep.* 124, 255
- Heske, A., Forveille, T., Omont, A., van der Veen, W. E. C. J., & Habing, H. J. 1990, *A&A*, 239, 173
- Huggins, P. J., & Glassgold, A. E. 1982, *ApJ*, 252, 201
- Hyland, A. R., Beckwith, E. E., Frogel, J. A., & Neugebauer, G. 1972, *A&A*, 16, 204
- Iben, I., Jr., & Renzini, A. 1983, *ARA&A*, 21, 271
- IRAS* Catalogs and Atlases: Explanatory Supplement. 1988, ed. C. A. Beichman, G. Neugebauer, H. J. Habing, P. E. Clegg, & T. J. Chester (Washington: GPO)
- Jones, T. J., Hyland, A. R., & Gatley, I. 1983, *ApJ*, 273, 660
- Jones, T. J., & Merrill, K. M. 1976, *ApJ*, 209, 509
- Jura, M. 1987, *ApJ*, 313, 743
- Knapp, G. R., & Morris, M. 1985, *ApJ*, 292, 640
- Knapp, G. R., Phillips, T. G., Leighton, R. B., Lo, K. Y., Wannier, P. G., & Wootten, H. A. 1982, *ApJ*, 252, 616
- Kratschmer, W., & Huffman, D. R. 1979, *Ap&SS*, 61, 195
- Lebofsky, M. J., Kleinmann, S. G., Reike, G. H., & Low, F. J. 1976, *ApJ*, 206, L157
- Leger, A., Gauthier, S., Defourneau, D., & Rouan, D. 1983, *A&A*, 117, 164
- Lockwood, G. W. 1970, *ApJ*, 160, L47
- Mathis, J. S., Rumble, W., & Norsieck, K. H. 1977, *ApJ*, 217, 425 (MRN)
- Merrill, K. M., & Soifer, B. T. 1974, *ApJ*, 189, L27
- Merrill, K. M., & Stein, W. A. 1976, *PASP*, 88, 294
- Netzer, N., & Knapp, G. R. 1987, *ApJ*, 323, 734
- Nguyen-Q-Rieu, Laury-Micholant, C., Winnberg, A., & Schultz, G. V. 1979, *A&A*, 75, 351
- Pendleton, Y. J. 1987, Ph.D. thesis, Univ. Calif. Santa Cruz
- Roche, P. F., & Aitken, D. A. 1984, *MNRAS*, 209, 33P
- Rowan-Robinson, M., & Harris, S. 1983, *MNRAS*, 202, 767
- Salpeter, E. E. 1974, *ApJ*, 193, 585
- Schutte, W., & Tielens, A. G. G. M. 1989, *ApJ*, 343, 369
- Simon, T., Morrison, D., & Cruikshank, D. P. 1972, *ApJ*, 177, L17
- Sivagnanam, P., Le Squeren, A. M., Foy, F., & Tran Minh, F. 1989, *A&A*, 211, 341
- Strecker, D. W., & Ney, E. P. 1974, *AJ*, 79, 797
- te Lintel Hekkert, P., Versteeg-Hensel, H. A., Habing, H. J., & Wiertz, M. 1989, *A&AS*, 98, 399
- Thomas, J. A., Robinson, G., & Hyland, A. R. 1976, *MNRAS*, 174, 711
- Tielens, A. G. G. M., & Allamandola, L. J. 1987, *Interstellar Process*, ed. D. J. Hollenbach & H. A. Thomason, Jr. (Dordrecht: Reidel)
- van de Hulst, H. C. 1981, *Light Scattering by Small Particles* (New York: Dover)
- van der Veen, W. E. C. J., & Habing, H. J. 1988, *A&A*, 194, 125
- van der Veen, W. E. C. J., & Rutgers, M. 1989, *A&A*, 226, 183
- Volk, K., & Kwok, S. 1988, *ApJ*, 331, 435
- Werner, M. W., Beckwith, S., Gatley, I., Sellgren, K., Berriman, G., & Whiting, D. 1980, *ApJ*, 239, 540
- Wilson, W. J., & Barrett, A. H. 1968, *Science*, 161, 778
- Wilson, W. J., Schwartz, P. R., Neugebauer, G., Harvey, P. M., & Becklin, E. E. 1972, *ApJ*, 177, 523